The piercing of the Atlantic Layer by an Arctic shelf water cascade in an idealised study inspired by the Storfjorden overflow in Svalbard

Fred Wobus[a,*], Georgy I. Shapiro[a,b], John M. Huthnance[c], Miguel A. M. Maqueda[c]

[a] *School of Marine Science and Engineering, University of Plymouth, PL4 8AA, UK, Tel.: +44-1752-586100*
[b] *Shirshov Institute of Oceanology, 36 Nahimovski prospect, Moscow, 117997, Russia*
[c] *National Oceanography Centre, Joseph Proudman Building, 6 Brownlow Street, Liverpool, L3 5DA, UK*

Abstract

A plume of dense brine-enriched water, resulting from sea ice production in the Storfjorden polynya (Svalbard), cascades into Fram Strait and encounters a layer of warm, saline Atlantic Water. In some years the plume continues to sink into the deep Fram Strait while in other years it remains at Atlantic Layer depths. It has been unclear what parameters control whether the plume pierces the Atlantic Layer or not.

We use a high-resolution 3-D numerical ocean model (NEMO-SHELF) to simulate an idealised scenario where a cascade descends a conical slope into an ambient 3-layer stratification. The model uses 1 km horizontal resolution and a blend of s- and z coordinates with 42 layers in the vertical arranged to resolve the plume at the bottom. We vary the salinity 'S' and the flow rate 'Q' of the simulated Storfjorden overflow to investigate both strong and weak cascading conditions. In agreement with observations the model reproduces three regimes: (i) the plume is arrested within or just below the Atlantic Layer, (ii) the plume pierces the Atlantic Layer and continues to the bottom of the slope and an intermediate regime (iii) where a portion of the plume detaches from the bottom, intrudes into the Atlantic Layer while the remainder continues its downslope propagation. For our idealised case the cascading regime can be predicted from the initial values of S and Q. In those model experiments where the initial density of the overflow water is considerably greater than of the deepest ambient water mass we find that

*Corresponding author:
Email address: fred.wobus@plymouth.ac.uk (Fred Wobus)

a cascade with high initial S does not necessarily reach the bottom if Q is low. Conversely, cascades with an initial density just slightly higher than the deepest ambient layer may flow to the bottom if the flow rate Q is high. A functional relationship between S/Q and the final depth level of plume waters is explained by the flux of potential energy (arising from the introduction of dense water at shallow depth) which, in our idealised setting, represents the only energy source for downslope descent and mixing.

Keywords: Arctic Ocean, Dense water cascading, Stratified flows

1. Introduction

Winter cooling and sea ice formation forms large amounts of brine-enriched shelf water over the vast shelves in the Arctic Ocean. Plumes of dense shelf water eventually spill over the continental shelf edge and flow down the slopes as dense water cascades (see e.g. Ivanov et al., 2004, for an overview of known cascading locations in the Arctic and other oceans). During their descent the cascading plumes entrain the ambient water, lose their initial density gradient and eventually disperse laterally into the ambient stratification (e.g. Aagaard et al., 1985; Jungclaus et al., 1995; Shapiro et al., 2003).

Dense water formation is particularly intense in coastal polynyas, which are estimated to produce a total of 0.7-1.2 Sv($1\,\mathrm{Sv} \equiv 10^6\,\mathrm{m^3 s^{-1}}$) of dense water over the entire Arctic ocean (Cavalieri and Martin, 1994), making this process of deep water formation comparable to open ocean convection in the Greenland Sea (Smethie et al., 1986). The dense waters formed on the shelves thus significantly influence the heat and salt balance of the entire Arctic Ocean (Aagaard et al., 1985). Cascading also contributes to the maintenance of the cold halocline layer (Aagaard et al., 1981) and the replenishment of intermediate and deep Arctic waters (Rudels and Quadfasel, 1991; Rudels et al., 1994).

A well-known site of dense water formation and subsequent cascading is the Storfjorden, located between 76 °30”–78 °30” N and 17 °–22 ° W in the south of the Svalbard archipelago (Fig. 1). Each winter, intense sea ice production and brine-rejection in a recurring latent-heat polynya in Storfjorden forms significant amounts of dense water (Schauer, 1995; Haarpaintner et al., 2001; Skogseth et al., 2005b) which eventually spill over the sill located at approx. 77 °N and 19 °E at a depth of 115 m (Skogseth et al., 2005a; Geyer et al., 2009). Near the sill the overflow plume encounters the relatively fresh

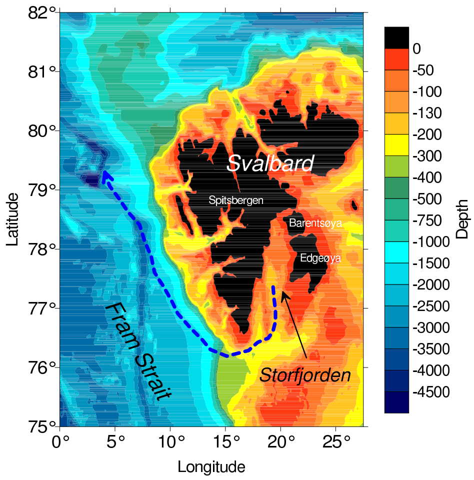

Figure 1: Map of the Storfjorden in the Svalbard archipelago. The pathway of the overflow plume (blue arrow) is approximated from observations (Quadfasel et al., 1988) and modelling (Fer and Ådlandsvik, 2008; Akimova et al., 2011). Bathymetry from IBCAO 2.23 (Jakobsson et al., 2008).

and cold East Spitsbergen Water (ESW) which mainly reduces its salinity (Fer et al., 2003). The flow is then channelled through the Storfjordrenna on a westwards path, before it bends northwards to follow the continental slope of western Spitsbergen (Quadfasel et al., 1988; Fer and Ådlandsvik, 2008; Akimova et al., 2011, see Fig. 1).

The lighter fractions of the overflow water remain within the depth range of the Atlantic Water (approx. 200-500 m) and contribute to the northward freshening and cooling of the West-Spitsbergen Current (Schauer, 1995; Saloranta and Haugan, 2004), while the densest fractions pass through the Atlantic Layer where they gain heat but lose only little salt as the salinity of the Atlantic Water is close to that of the plume at this stage (35.0 compared to 35.1, see Quadfasel et al., 1988).

Shelf water of Storfjorden origin has been observed in the deep Fram Strait (at >2000 m) on several occasions, in 1986 (Quadfasel et al., 1988), 1988 (Akimova et al., 2011) and 2002 (Schauer et al., 2003). In observations at other times the cascade was arrested within the depth range of the Atlantic Layer, e.g. in 1994 (Schauer and Fahrbach, 1999) when it was observed no deeper than 700 m.

The observations thus reveal two regimes - (i) the plume pierces the Atlantic Layer and penetrates into the deep Fram Strait or (ii) the plume is arrested within the layer of Atlantic Water. The eventual depth of the cascaded waters has a proven effect on the maintenance of the Arctic halocline (when the plume is arrested) and (when piercing occurs) the ventilation of the deep Arctic basins (Rudels et al., 2005).

It has been unclear what parameters control the regime of the plume. Can we predict when the cascade will be arrested and when it will pierce the Atlantic Water from the knowledge of the ambient conditions and the source water parameters alone? How does the cascading regime respond to changes in the flow rate and/or the salinity of the overflow waters? Here we present a modelling study to answer these questions.

2. Methods

2.1. Model geometry and water masses

We model an idealised ocean basin which has at its centre a conical slope with an angle of $1.8\,^\circ$ which captures the bathymetry of Svalbard's western continental slope. The depth ranges from 115 m at the flattened tip of the cone to 1500 m at its foot. The conical geometry acts like a near-infinite slope wrapped around a central axis (Fig. 2). An advantage of a conical slope is that rotating flows can be studied for long periods of time without the plume reaching any lateral boundary, thus avoiding possible complications with boundary conditions in a numerical model. The maximum model depth of 1500 m is shallower than Fram Strait, but deep enough to observe whether the modelled plume has descended past the depth range of the Atlantic Layer.

The ambient conditions in the model ocean are based on the three main water masses that the descending plume encounters successively (cf. Fer and Ådlandsvik, 2008). The surface layer of East Spitsbergen Water (ESW) is typical of winter conditions, the middle layer of Atlantic Water (AW) is typical of early spring and the deep layer of Norwegian Sea Deep Water (NSDW) is based on late spring climatology (World Ocean Atlas 2001, Conkright et al., 2002). Ambient waters (Fig. 2) are stagnant at the start of each run and no momentum forcing is applied.

A fourth water mass, which we call here Storfjorden overflow water (SFOW), is introduced as a continuous flow at the shallowest part of the slope in 115 m (Fig. 2), which is the sill depth of the Storfjorden. As SFOW is the result of sea ice formation and brine rejection its temperature is always set to approximate freezing point, $T = -1.95\,^\circ$C. The injected flow is further characterised by a prescribed salinity S and flow rate Q which vary between model runs,

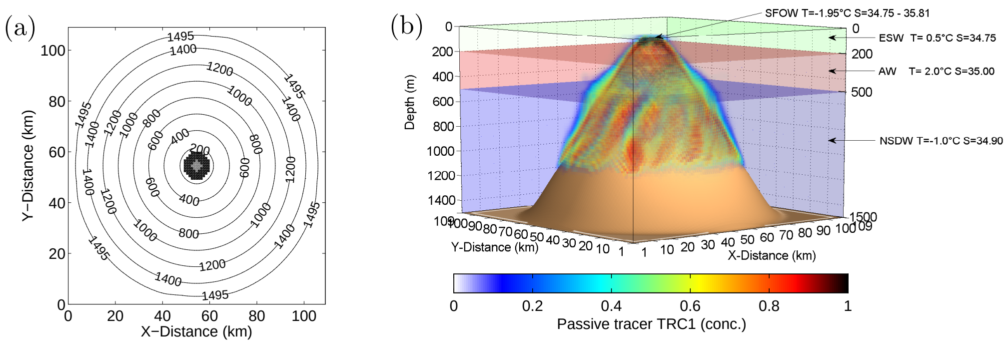

Figure 2: (a) Depth contours of the model bathymetry with a conical slope at its centre. The grid cells of the dense water inflow (solid black) are arranged around a central 'island' (grey). (b) 3-D schematic of the model domain with the ambient water masses in their initial state: East Spitsbergen Water (ESW), Atlantic Water (AW), Norwegian Sea Deep Water (NSDW) and Storfjorden Overflow Water (SFOW). The plume of SFOW during one of the numerical experiments is shown as a volume rendering of passive tracer concentration (colour scheme below plot).

which aim to represent previously observed conditions. Using observations of the densest waters found within the fjord during 1981 to 2002 (Skogseth et al., 2005b) we vary the inflow salinity S from 34.75 to 35.81. The flow rate Q is varied from 0.01 to 0.08 Sv, based on observations at the sill of a mean volume transport of 0.05 to 0.08 Sv (Schauer and Fahrbach, 1999; Skogseth et al., 2005a; Geyer et al., 2009). In the present study we do not attempt to model the dense water formation process itself. The flow rate Q and the salinity S of the simulated overflow waters are intended to capture the parameters of the SFOW behind and at the sill.

2.2. Model setup

We employ the NEMO-SHELF model (O'Dea et al., 2012) at 1 km resolution with a 109×109 grid in the horizontal and 42 levels in the vertical. The baroclinic time step is 40 s with time splitting for the barotropic component every 20 steps.

O'Dea et al. (2012) describes in detail the modifications to NEMO (Madec, 2008) for use in shelf seas and regional studies. We include here only a brief summary of the differences as well as its configuration specific to this study and our own modifications to the NEMO-SHELF code.

A key departure of the NEMO shelf code from the open ocean is the use of a terrain-following s-coordinate discretisation in the vertical instead of z-coordinates. The s-coordinate system is well suited to the modelling of

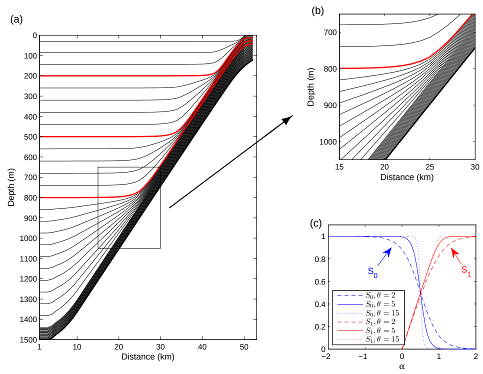

Figure 3: (a) The s_h-coordinate system shown as a cross-section through the centre of the model domain. The box is magnified in (b) which shows that out of a total of 42 levels, at least 16 are reserved for a bottom boundary layer of constant thickness. The s_h-levels (i.e. virtual seabeds, in red) are placed at certain depth levels to flatten s-levels in the interior and coincide with isopycnals in the ambient water. Panel (c) shows the smoothing functions S_0 and S_1 (Eqns. (A.2) and (A.3) respectively) with different values for the smoothing parameter θ (see Appendix A).

density currents (see e.g. Wobus et al., 2011), but the horizontal boundaries between ambient layers (Fig. 2) would suffer numerical diffusion over areas of sloping topography where s-levels intersect the isopycnals at an angle. We therefore modify the vertical coordinate system because neither the traditional s-coordinate nor z-coordinate systems suit our scenario where strong gradients are orientated vertically (in the ambient water) and also normal to the slope (at the upper plume boundary). The approach of blending s- and z-coordinates in this study can be traced back to Enriquez et al. (2005) who used a traditional s-coordinate stretching function (Song and Haidvogel, 1994) but achieved horizontal s-levels over the interior of a basin by capping its bathymetry. Ivanov (2011) changed the traditional s-coordinate formulation by introducing virtual seabeds at certain depth levels to maintain horizontal s-levels closer to the slope. The levels designated as virtual seabeds (here called "s_h-levels") follow the terrain only at shallower depths, while maintaining a prescribed depth over deep bathymetry.

Our modified s_h-coordinate system[1] refines the Ivanov (2011) approach by smoothing the transition between horizontal and terrain-following s-levels

[1]subscript 'h' denotes that some levels are horizontal.

(Fig. 3). The smoothing reduces errors in the calculation of the second derivative of the s-level slope. In this study we reserve 16 out of the 42 levels for a bottom layer of constant thickness (60 m). These bottom layer s-levels are always terrain-following with equidistant spacing to avoid any loss in vertical resolution with increasing depth (as is the case with the traditional s-coordinate stretching function). The algorithm is described in detail in Appendix A.

A second difference in NEMO-SHELF is the use of a non-linear free surface formulation with variable volume (Levier et al., 2007) which is advantageous for this study as it allows to account for the injection of dense water using the model's river scheme. The 'river' injection grid cells are arranged over a 50 m-thick layer above the bottom at 115 m depth in a 3 km-wide ring around a central 'island' of land grid cells (Fig. 2a). The island's vertical walls avoid a singularity effect at the centre of rotation and prevent inflowing water from sloshing over the cone tip. A constant flow rate Q (in $\mathrm{m^3 s^{-1}}$) of water at a given salinity S is evenly distributed over all injection grid cells. The inflowing water is marked with a passive tracer 'PTRC' (using the MYTRC/TOP module) by continually resetting the PTRC concentration to 1.0 at the injection grid cells.

Thirdly, NEMO-SHELF includes the Generic Length Scale (GLS) turbulence model (Umlauf and Burchard, 2003) which we use in its k-ϵ configuration with parameters from Warner et al. (2005) and Holt and Umlauf (2008). The scheme's realistic vertical diffusivity and viscosity coefficients give confidence to the accurate representation of the frictional Ekman layer within the plume. The advection scheme in the vertical is the Piecewise Parabolic Method (vPPM, by Liu and Holt, 2010). The high precision Pressure Jacobian scheme with Cubic polynomial fits which is particularly suited to the s-coordinate system is used as the horizontal pressure gradient algorithm (kindly made available by H. Liu and J. Holt, NOCL).

For the parametrisation of the subgrid-scale horizontal diffusion of tracers and momentum we use the Laplacian (harmonic) operator with constant diffusivity coefficients ($A_{h_t} = A_{h_m} = 3.0\,\mathrm{m^2 s^{-1}}$ for tracers and momentum respectively). Care is taken to separate the large lateral diffusion from the tiny diffusion in the diapycnal direction (see Griffies, 2004, for a discussion) by activating the rotated Laplacian operator scheme. For this study we modify the calculation of the slope of rotation to blend the slope of isopycnal surfaces with the slope of surfaces of constant geopotential depending on the intensity of the background stratification. This approach, which is described in detail in Appendix B, was especially devised for our ambient conditions where the calculation of isopycnal surfaces within a well-mixed ambient layer may lead to unphysical slope angles that cause lateral diffusion to ‘leak’ into the sensitive vertical diffusion.

Lastly, we implement a no-slip boundary condition at the bottom (rather than the quadratic drag law, which is often used as standard bottom friction parametrisation in ocean models) and prescribe a fine vertical resolution near the bottom (relative to the Ekman layer height) to explicitly resolve the velocity profiles in the frictional bottom boundary layer. Resolving bottom friction, rather than parametrising it, has been demonstrated to significantly increase the accuracy of modelling gravity currents in a rotating framework (Wobus et al., 2011).

2.3. Model validation

Prior to the model experiments described here we applied the NEMO-SHELF code (Section 2.2) to the model experiments of Wobus et al. (2011) and successfully validated the results against the laboratory experiments by Shapiro and Zatsepin (1997). NEMO was able to match the laboratory results with the same degree of confidence as the POLCOMS model of Wobus et al. (2011). In an injection-less control run we found spurious velocities to remain well below $1\,\mathrm{cm\,s^{-1}}$ indicating the accuracy of the horizontal pressure gradient scheme. Numerical diffusion at horizontal isopycnals was also effectively controlled.

We would like to add a brief note on the condition of ”hydrostatic inconsistency” which was brought to the attention of the ocean modelling community by Haney (1991) and others. Written for a constant slope angle θ and bathymetric depth D they state that if $R = \left|\frac{\sigma}{D}\frac{\Delta x\, tan\theta}{\delta\sigma}\right|$, the model should satisfy $R \leq 1$ for the finite difference scheme to be hydrostatically consistent and convergent. Mellor et al. (1994), however, showed that this condition strongly depends on the exact nature of the numerical scheme, and convergent results can be obtained even for values $R \gg 1$. In fact, in the POLCOMS model of Wobus et al. (2011) the worst-case was $R = 101$, yet a close agreement was achieved between model and laboratory experiments. In the present study we get $R \leq 8$, which adds to our confidence in the results.

3. Results and discussion

We perform a series of 45 model runs using the NEMO model setup described in Section 2. The dense water parameters are varied while the initial conditions are identical in all runs. All runs are integrated over a duration of 90 days.

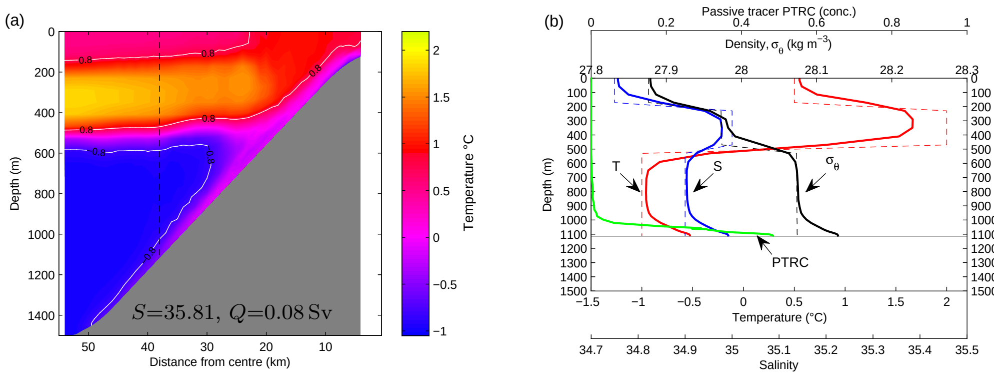

Figure 4: (a) Temperature section (after 24 days) in a model run with strong cascading. The isotherms drawn at -0.8 and $0.8\,°$C (white lines) are an approximate boundary between the cascade and ambient water where their slope is parallel to the bottom. The vertical dashed line marks the sampling of the vertical profiles in (b): temperature (red), salinity (blue), density (black) and PTRC concentration (green). Initial conditions are shown as dashed lines.

With the start of each experiment the injected dense water forms a plume of approximately circular shape which spreads downslope. At the leading edge of the plume wave-like baroclinic instabilities gradually develop into meanders and eddies reaching a width of $8 - 12$ km. At depth, where the Rossby radius of deformation is approx. $R_o = 4$ km, the size of these features thus conforms to the expected horizontal length scale of $2 \times R_o$ to $3 \times R_o$ (Griffiths and Linden, 1982).

On its descent the plume successively encounters East Spitsbergen Water (ESW) near the sill, then Atlantic Water (AW) at intermediate depths and finally Norwegian Sea Deep Water (NSDW). Fig. 4a shows a temperature cross-section where the plume has penetrated all three ambient layers and reached the bottom of the slope. A thin warm layer above the bottom is emphasised by the $-0.8\,°$C isotherm parallel to the slope between 700 and 1400 m. This is a sign of the plume warming as it passes through warm AW during its descent yet retaining a sufficient density contrast to continue to greater depths. This signature of a near-bottom temperature and salinity maximum was observed in Fram Strait by Quadfasel et al. (1988).

The cascade in Fig. 4a also drives warm water from the Atlantic Layer to the surface. The upwelling effect of a cascade is not caused by continuity alone (ambient water moving upwards to replace descending colder water) as it would not be induced if the same amount of dense water were injected in the deepest layer. Upwelling is also a result of velocity veering in the bottom and interfacial Ekman layers as shown by Shapiro and Hill (1997) in a $1\frac{1}{2}$-layer model and by Kämpf (2005) in laboratory experiments.

The ambient waters in Fig. 4a are also modified as a result of the dense water flow. The surface layer of ESW has been displaced from the inflow area and the Atlantic Layer shows signs of cooling near the slope. The 0.8 °C isotherms which may serve as both shallow and deep boundaries of the Atlantic Layer have been displaced upwards indicating an upwelling of warm water towards the surface. This is in contrast to the control run without any dense water injection where all isotherms remain horizontal.

The vertical profiles at a location in just over 1100 m depth (Fig. 4b) show the plume as a density maximum above the bottom. A similar gradient is evident in the temperature and salinity profiles. The PTRC concentration is used to determine the plume height h_F in the following section.

3.1. Cascading regimes

Our numerical experiments reveal three regimes of cascading: (i) "arrested" - the plume remains within or just below the Atlantic Layer (Fig. 5a), (ii) "piercing" - the plume pierces the Atlantic Layer and continues to the bottom of the slope (Fig. 5b) and an intermediate regime (iii) "shaving" - where a portion of the plume detaches off the bottom, intrudes into the Atlantic Layer while the remainder continues its downslope propagation (Fig. 5c). The latter regime was so named by Aagaard et al. (1985) who inferred it from observations. The arrested regime was observed in 1994 (Schauer and Fahrbach, 1999), while the piercing regime was observed in 1986 (Quadfasel et al., 1988), in 1988 (see Akimova et al., 2011) and in 2002 (Schauer et al., 2003).

For the 'arrested' and 'piercing' regimes we examine the thickness of the plume h_F which is derived from vertical profiles of PTRC as the height above the bottom where the concentration drops below 50% of the value reached at the seabed. Values are averaged in space along the plume edge and up to

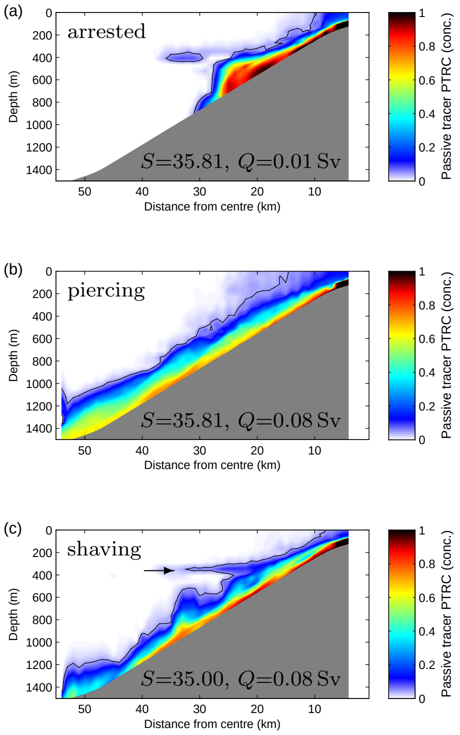

Figure 5: Cross-section of tracer concentration after 90 days from experiments with three different combinations of SFOW inflow salinity S and flow rate Q. In all cases the initial SFOW density is higher than the density of NSDW in the bottom layer. The concentration PTRC = 0.05 is shown as a solid contour.

10 km behind the plume front and in time over the 20 days before the flow reaches 1400 m depth.

The plume thickness in our model varies between 30 and 228 m, which is generally greater than observations in Fram Strait of a 10-100 m thick layer of Storfjorden water at depth (Quadfasel et al., 1988). The disparity appears smaller for our model than in modelling studies by Jungclaus et al. (1995) and Fer and Ådlandsvik (2008) who reported $h_F \approx$ 200-400 m. However, it should be noted that the plume thickness is very sensitive to the chosen tracer threshold value, and our plume thickness could fall into the same range as Fer and Ådlandsvik (2008) if we used a different threshold. We therefore do not overemphasise the detailed comparison of the modelled plume height with actual observations of the Storfjorden plume as many aspects of our model setup are idealised and not designed to replicate observed conditions.

The absolute plume thickness h_F is normalised by the Ekman depth H_e defined here as $H_e = \sqrt{2\nu/f \cos\theta}$ for a given slope angle θ and the vertical viscosity ν (calculated here by the GLS turbulence closure scheme) which is averaged over the core of the plume. The vertical diffusivity κ is also shown to assess the vertical Prandtl number $Pr_v = \nu/\kappa$ which is $\approx \mathcal{O}(1)$.

The Entrainment ratio is calculated as $E = w_e/u_F$, where w_e is the entrainment velocity $d\,h_F/dt$ (Turner, 1986) and $u_F = dL/dt$ is the downslope speed (L is the distance of the plume edge from the inflow) of the flow. E is calculated over the time taken by the flow until it has reached 1400 m depth (or until the end of the experiment if this depth isn't reached). The results for both subsets of experiments are summarised in Table 1.

Table 1: Characteristics of the plume in the 'arrested' and 'piercing' regime: plume height h_F, vertical viscosity ν, vertical diffusivity κ, Ekman depth H_e, normalised plume height $\frac{h_F}{H_e}$ and entrainment ratio E. One standard deviation is given in brackets.

	arrested (10 runs)	piercing (16 runs)	
h_F	166 (43)	44 (11)	m
ν	9.2 (2.9)	5.7 (0.4)	$\times 10^{-3}\,\mathrm{m^2 s^{-1}}$
κ	9.6 (4.2)	6.3 (0.4)	$\times 10^{-3}\,\mathrm{m^2 s^{-1}}$
H_e	11 (1.7)	9 (0.3)	m
$\frac{h_F}{H_e}$	14.9 (4.2)	4.8 (1.0)	
E	5.4×10^{-3} (2.6×10^{-3})	0.33×10^{-3} (0.29×10^{-3})	

Values for vertical viscosity ν and Ekman depth H_e are typical for oceanic scales (e.g. Cushman-Roisin and Beckers, 2011) and they are similar in both regimes. However, the plume height h_F differs considerably between both sets of experiments. A piercing plume is on average 44 m thick towards the bottom end of the flow compared to 166 m in experiments where the plume is arrested. An explanation is found in the entrainment ratio E which changes with the depth level of the plume head and thus varies through time. The value of E is larger while the plume head is at the depth level of a density interface in the ambient waters (which is a considerable portion of the total experiment time in arrested runs). Its value is smaller during the plume's descent through a homogenous layer of ambient water (as it does for the majority of the experiment time in piercing runs).

Based on buoyancy considerations alone one could expect that the incoming plume with a density greater than the density of the bottom layer (in our case for S>34.85) should always penetrate into that layer. However, our results show that this is not the case because of mixing processes that result in density changes of the plume as it progresses downslope over time.

3.2. Rate of descent

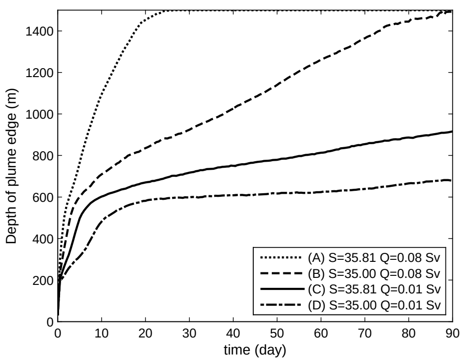

Figure 6: Downslope progression of the plume edge for four example runs with varying S and Q.

In this section, we examine the downslope propagation of the plume. Fig. 6 shows the depth of the plume edge over time calculated from the deepest appearance of a concentration PTRC$\geq$0.05 in the bottom model level. The plume speed slows over time, which is due to (i) the increase in diameter of the leading edge as the plume progresses further down the cone which causes a thinning of the plume that in turn increases the effect of drag on the plume and (ii) the mixing of the plume with ambient waters resulting in a gradual decrease in density contrast, especially upon encountering the transition between ambient water masses at 200 and 500 m. The plume in run D (S=35.00, Q=0.01 Sv, Fig. 6) slows noticeably at the 200 m interface (between ESW-AW), while the other runs are less affected at this depth level. In all runs the plume is slowed upon encountering the 500 m depth level of the AW-NSDW interface, but the plume in run A which has the strongest inflow (S=35.81, Q=0.08 Sv) is least affected and reaches the bottom of the slope after only 20 days. Fig. 6 demonstrates that plumes with different initial parameters spend varying lengths of time flowing through and mixing with the different layers of ambient water which affect the final fate of the plume (see sections 3.3 and 3.4).

At this point it's appropriate to include a note on the relationship between the downslope speed of the plume front and its alongslope speed. For each model run the downslope speed u_F is calculated for the latter part of the experiment when the descent rate is roughly constant - from 20 days (or when the plume edge has passed 800 m depth, if earlier) until the end of the model run or when the plume edge has reached 1400 m (*cf.* Fig. 6). For the same time period we also derive the reduced gravity $g' = g\frac{\Delta\rho}{\rho_0}$ based on the density gradient across the plume front. Experiments where the plume is arrested and g' is close to 0 or even negative (due to the overshoot at the front) are excluded.

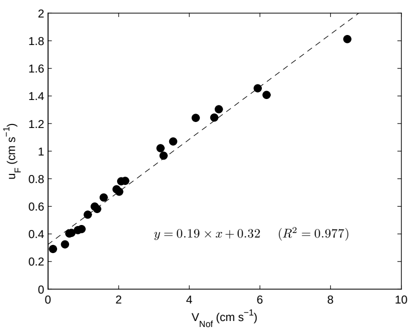

Figure 7: Correlation between the alongslope geostrophic velocity scale ($V_{Nof} = \frac{g'}{f}\tan\theta$) and the downslope velocity of the plume front (u_F). Data is plotted for runs with a positive density gradient at the plume front.

Fig. 7 compares the downslope velocity component u_F to the alongslope component $V_{Nof} = \frac{g'}{f} \tan\theta$ (Nof, 1983), where $f = 1.415{\times}10^{-4}\,\mathrm{s}^{-1}$ is the Coriolis parameter and $\theta = 1.8\,^\circ$ is the slope angle. An overall average ratio of all downslope and alongslope velocities from all 45 runs is calculated using linear regression as $\frac{u_F}{V_{Nof}} = 0.19$ ($R^2 = 0.977$) which is surprisingly close to the ratio of $\frac{u_F}{V_{Nof}} = 0.2$ given by Shapiro and Hill (1997) as a simplified formula for the quick estimation of cascading parameters from observations. The Killworth (2001) formula for the rate of descent of a gravity current can be written for our slope angle ($\theta = 1.8\,^\circ$) as $u_F = \frac{1}{400} \frac{V_{Nof}}{\sin\theta} = 0.08\, V_{Nof}$ making our modelled downslope velocities approximately 2.4× greater than Killworth's prediction.

Shapiro and Hill (1997) developed their formula for a $1\frac{1}{2}$-layer model of cascading on a plane slope and assuming a sharp separation between ambient water and a plume with a normalised thickness of $\frac{h_F}{H_e} \approx 1.78$. Our ratio of $\frac{u_F}{V_{Nof}} = 0.19$ was computed for those runs with a positive density gradient at the plume front, which naturally puts them in the 'piercing' category. The normalised plume height averaged over those runs is $\frac{h_F}{H_e} = 4.7$, which indicates a more diluted plume than assumed for the Shapiro and Hill (1997) model.

Wobus et al. (2011) studied the flow of dense water down a conical slope in absence of density gradients in the ambient water. They found that prescribing enhanced vertical diffusion slows the downslope progression of the plume, while prescribing enhanced vertical viscosity increases downslope transport (given sufficient supply of dense water). The agreement with the descent rate prediction of Shapiro and Hill (1997) was shown by Wobus et al. (2011) not to be limited to cascades with a sharp interface and a thin plume with $h_F \sim \mathcal{O}(H_e)$, but also applicable to thick and diffuse plumes as long as the vertical diffusivity κ and viscosity ν are of approximately the same magnitude (i.e. a vertical Prandtl number of $Pr_v \sim \mathcal{O}(1)$). This study confirms the Shapiro and Hill (1997) descent rate formula in a model using the GLS turbulence closure scheme (rather than prescribed turbulence). The agreement in Fig. 7 is explained by plumes of the 'piercing' regime of our experiments meeting the aforementioned Prandtl number criterion (see Table 1).

3.3. Mixing characteristics

On its downslope descent the plume (SFOW) mixes with and entrains three ambient water masses (ESW, AW and NSDW). Entrainment implying a volume increase is based on a potentially arbitrary distinction between plume water and ambient water which could result in imprecise heat and salt budgets. In the following we therefore concentrate on the mixing process where these budgets remain well defined. Fig. 8 shows θ-S diagrams that trace the water properties down the slope at the end of each experiment (after 90 days). The θ-S values are plotted for the bottom model level at increasing depths from inflow region down to 1500 m. We show the θ-S properties for two experiments series: Q is constant and S varies (Fig. 8a), and Q varies and S is constant (Fig. 8b).

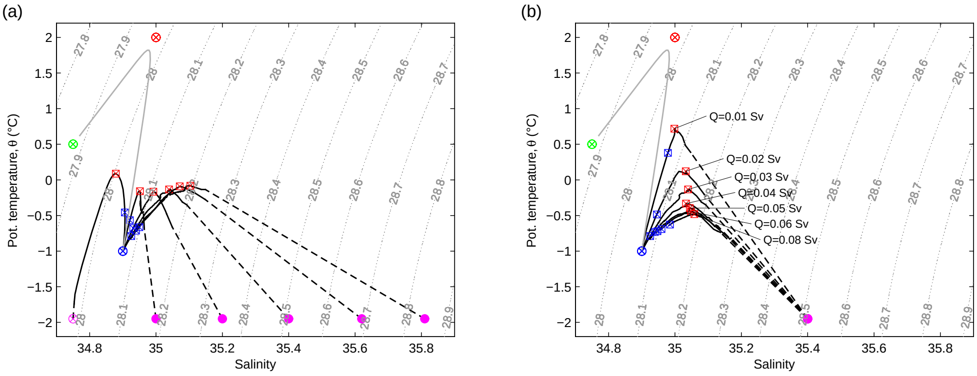

(a) varying S, Q=0.03 Sv (b) S=35.40, varying Q

Figure 8: Downslope evolution of θ-S properties in the bottom model level on the slope. Curves are plotted for two series of model runs after 90 days: (a) varying inflow salinity S and (b) varying flow rate Q. The four different water masses in the model's initial conditions are indicated by crossed circles: green, ESW; red, AW; blue, NSDW; cyan, SFOW. Filled cyan dots indicate SFOW that is denser than any ambient waters. The temperature maximum on the slope is marked by a crossed red square, while the deepest penetration of passive tracers with concentration PTRC>0.05 is marked by a blue square. The mixing within the injection grid cells is shown by the dashed black line. The faint gray curve is from a run without any injection (Q=0) for comparison.

The dashed portion of the mixing curves in Fig. 8 shows that a considerable amount of mixing takes place within the injection grid cells. Any water introduced into the model is immediately diluted by ambient water. These processes take place over a very small region of the model and are not considered any further. Instead we focus on the common feature of all curves in Fig. 8: the temperature rises to a temperature maximum (marked by red squares) due to the plume's mixing with warm Atlantic Water. A very similar mixing characteristic was described by Fer and Ådlandsvik (2008) for a single overflow scenario (S = 35.3, $T = -1.9\,^{\circ}$C, Q_{avg} = 0.07 Sv) in a 3-D model study using ambient conditions similar to ours.

Amongst the series with constant Q=0.03 Sv (Fig. 8a) only the weakest cascade (inflow salinity S=34.75) retains traces of ESW in the bottom layer after 90 days. In the experiments with more saline inflow ($S\geq$35.00), the θ-S curve in Fig. 8a only spans three water masses - SFOW, AW and NSDW - while ESW is no longer present near the seabed. The salinity at the temperature maximum is nearly identical (red squares in Fig. 8a) for runs with the same flow rate Q.

The experiments with a constant inflow salinity S (Fig. 8b) reveal that as Q increases the temperature maximum drops. At high flow rates the plume water is warmed to a lesser degree by the warm ambient water due to a larger volume of cold water entering the system.

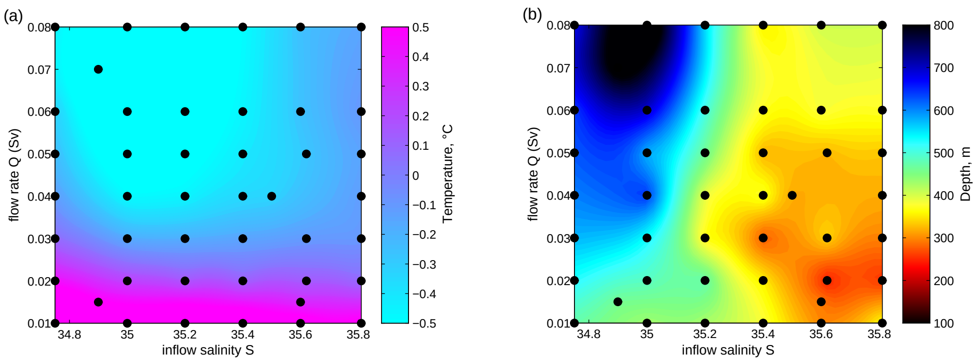

Figure 9: Characteristics of the temperature maximum in the bottom model level after 90 days is plotted against forcing parameters S and Q for all 45 experiments. (a) shows the temperature of the temperature maximum (in °C) and (b) shows the depth (in m) at which it occurs.

We will now analyse the combined effect of varying both S and Q, and also consider the depth at which the temperature maximum occurs. The plume's mixing with warmer ambient waters (especially the Atlantic Water) warms the initially cold flow of dense water and also changes the depth distribution of temperature.

For all model runs we determine the temperature maximum and depth of the temperature maximum found in the bottom model level at the end of each experiment. The results are plotted against S and Q to investigate the full range of forcing parameters for all model runs. In Fig. 9 each experiment is marked by a black dot at a modelled combination of S and Q and the temperature maximum (in Fig.9a) and its depth (in Fig. 9b) are shaded as coloured contours that span the S-Q space.

Fig. 9a shows that the magnitude of the temperature maximum (in °C) is primarily dependent on Q and almost independent of S, which confirms the interpretation of Fig. 8 for a wider range of forcing parameters. Cascades with low flow rates ($Q \leq 0.02$ Sv) are warmed by the ambient water to 0.2 °Cand above, while at higher flow rates ($Q \geq 0.03$ Sv) the cold cascade lowers the temperature maximum below 0 °C.

The flow rate dependence of the maximum bottom temperature in Fig. 9a can be explained by the different thermal capacity of the volume of plume water as Q changes, compared to the unchanged thermal capacity of the Atlantic Water. The salinity dependence of the depth of the temperature maximum in Fig. 9b is related to the salinity being the main driver of density at low temperatures. Plumes of lower salinity are thus less dense, causing them to advance downslope at slower speeds. A slowly descending plume remains in the Atlantic Layer for longer and more AW is mixed into the plume. Hence more warm Atlantic water gets advected downslope, causing the temperature maximum to occur at deeper depths in experiments with low S.

The mixing between the cold cascade and the warm ambient waters does not only lower the bottom-level temperature maximum, it also alters its depth which initially occurs within between 200 and 500 m at the start of each experiment. Fig. 9b shows that the depth of the temperature maximum has been displaced upslope (shallower than 400 m, shaded yellow) or downslope (deeper than 600 m, shaded blue) by the end of each experiment. In experiments where $S \leq 35.20$ the temperature maximum occurs at depths of 600 to 800 m while it remains at shallower depths of 200 to 400 m in experiments with $S > 35.20$. We conclude that the final depth of the temperature maximum is thus primarily dependent on the inflow salinity S.

By prescribing a varying salinity at the overflow we are able to recreate (in Fig. 8a) the schematic of Arctic cascading developed by Rudels and Quadfasel (1991), which is reproduced here in Fig. 10. Owing to the similarity in the ambient conditions and comparable parameters at the simulated overflow, the shape of the θ-S curve and the magnitude of the temperature maximum are in good agreement with this generalisation.

The results in this section expand on the Rudels and Quadfasel (1991) schematic and describe the response in the mixing to variations in volume

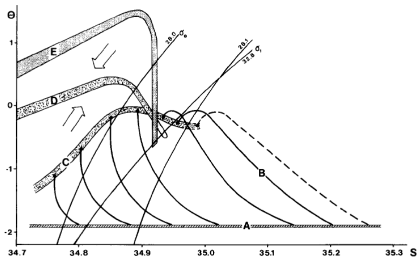

Figure 10: Schematic of the downslope evolution of θ-S properties of a dense water plume (from Rudels and Quadfasel, 1991). The mixing curves for source waters of different salinities (A) evolving (B) towards a temperature maximum due to the entrainment of Atlantic Water compare well with our Fig. 8a.

transport at the sill (see Fig. 8b). The maximum bottom temperature along the plume path is mainly a function of the flow rate (see Fig. 9a). The depth at which the temperature maximum occurs, on the other hand, is mainly a function of the inflow salinity.

To explain these results we consider the processes and factors affecting the temperature maximum on the slope: (i) downslope advection of AW by the plume, (ii) the plume's momentum arising from its density gradient, (iii) mixing of the plume with Atlantic Water, (iv) the smallness of the thermal expansion coefficient at low temperatures, and (v) the total thermal capacity of the plume water.

3.4. Depth penetration of the plume

In the following, we investigate how the salinity S and flow rate Q of the dense water inflow affect the plume's final depth level. We quantify the downslope penetration of SFOW by calculating how much passive tracer (PTRC) is resident within a given depth range by the end of the model run. The concentration of tracer is integrated over a given volume to give the mass of PTRC, M_{PTRC}. The penetration of the cascade into a given depth range is calculated as a percentage of M_{PTRC} within the given range compared to the total M_{PTRC} over the entire domain. A model run and its dense water supply can then be characterised according to the depth range containing more than 50% of PTRC that has been injected over 90 days.

In Fig. 11 we plot the results against S and Q for each of the 45 model runs. The final tracer percentage present within the given depth range is shaded in a contour plot where the S-Q combination of each experiment is marked by a black dot.

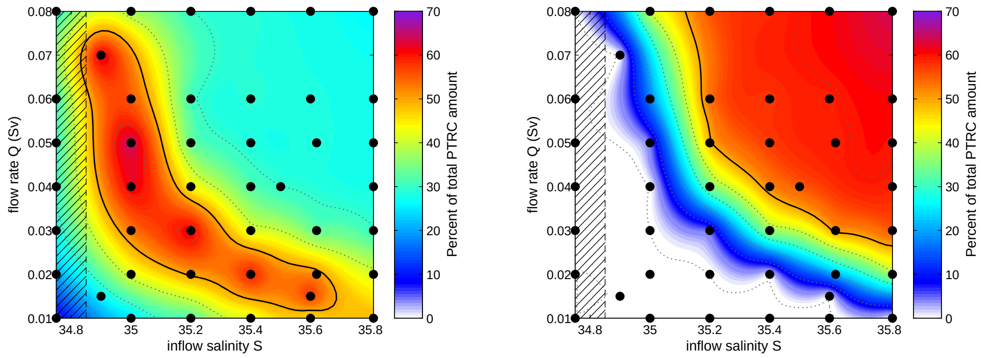

(a) $500\,\mathrm{m} \leq z \leq 1000\,\mathrm{m}$ (b) $z \geq 1000\,\mathrm{m}$

Figure 11: Presence of passive tracer (PTRC) (a) between 500 to 1000 m and (b) below 1000 m. Within the given depth range the percentage of tracer out of the total amount injected over 90 days is plotted against S and Q of all 45 model runs (black dots). The 50% contour is emphasised. The salinity range outside of the hatched area results in an initial plume density greater than the deepest ambient layer.

In those model runs where the majority of PTRC is present between 500 and 1000 m at the end of the experiment the plume has intruded into the Atlantic Layer and into the AW-NSDW interface, but not retained a strong enough density contrast to flow deeper. The combinations of S and Q producing this result are emphasised in Fig. 11a as the dots within the red shading indicating a tracer penetration greater than 50%. In the S-Q parameter space these runs are arranged in a curved band from low-S/high-Q via medium-S/medium-Q towards high-S/low-Q. In runs with lower S/lower Q (towards the lower left corner of the graph) the majority of the plume waters is trapped at shallower depths. In experiments with higher S/higher Q (towards the upper right corner of the graph) the plume reaches deeper as shown in Fig. 11b which is plotted for the presence of PTRC below 1000 m.

Fig. 11 provides a useful tool in classifying the prevailing regime in each experiment as ‘arrested’ (10 runs, Fig. 11a) or ‘piercing’ (16 runs, Fig. 11b) regarding the plume’s capacity to intrude into the Atlantic Layer or pass through it respectively. In the remaining experiments the plume either remains largely above the Atlantic Layer or the piercing ability is not clearly defined (which includes the ‘shaving’ regime).

The combinations of S/Q resulting in each of the regimes in Fig. 11 show that the initial density of the plume is not the only controlling parameter for the final depth of the cascade. At low flow rates, a plume which is initially denser than any of the ambient waters might not reach the bottom, while at high flow rates a lower initial density is sufficient for the plume to reach that depth. In the following section we explain the physics behind this result by considering the availability and sources of energy that drive the plume's descent.

3.5. Energy considerations

The final depth level of the plume depends on kinetic energy available for the downslope descent and the plume's mixing with ambient waters which dissipates energy. Even a closed system without any external forcing could contain available potential energy (APE, see Winters et al., 1995), but the APE in our model's initial conditions is negligible (as calculated using the algorithm described in Ilıcak et al., 2012) and remains constant during an injection-less control run. The only energy supply in our model setup (a closed system except for the dense water injection) thus derives from the potential energy of the injected dense water, which is released on top of lighter water. Any kinetic energy used for descent and mixing must thus have been converted from this initial supply of potential energy.

From the model output we derive the average potential energy (in $\mathrm{J\,m^{-3}}$) by integrating over the entire model domain:

$$PE = \frac{1}{V_{tot}}\, g \int_V \rho\, z\, dV \qquad (1)$$

where g is the acceleration due to gravity ($9.81\,\mathrm{m\,s^{-2}}$), V is the grid cell volume and $V_{tot} = \int dV$ is the total volume of the model domain.

The system's increase in potential energy over time is plotted in Fig. 12 for runs A, B and C (see Fig. 6). In all runs PE is shown to be increasing as dense water is continually injected. One of the runs (run A, high S/high Q) was shown in Fig. 11b to fall into the piercing regime, while run B (low S/high Q) corresponds to the shaving regime and the plume in run C (high S/low Q) is arrested. The piercing run achieves a notably higher total PE at the end of the experiment than in the other cases. We now consider only the final value of potential energy increase after 90 days (ΔPE) from the values derived at the start and end of each experiment:

$$\Delta PE = PE_{end} - PE_{start} \qquad (2)$$

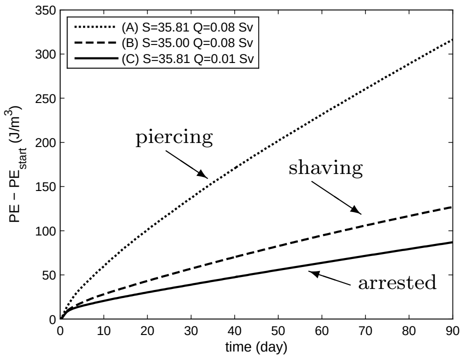

Figure 12: Increase over time in potential energy (PE) relative to the PE_{start} at the beginning of the experiment for three example runs varying S and Q. The labels point out the cascading regime (see Fig. 5).

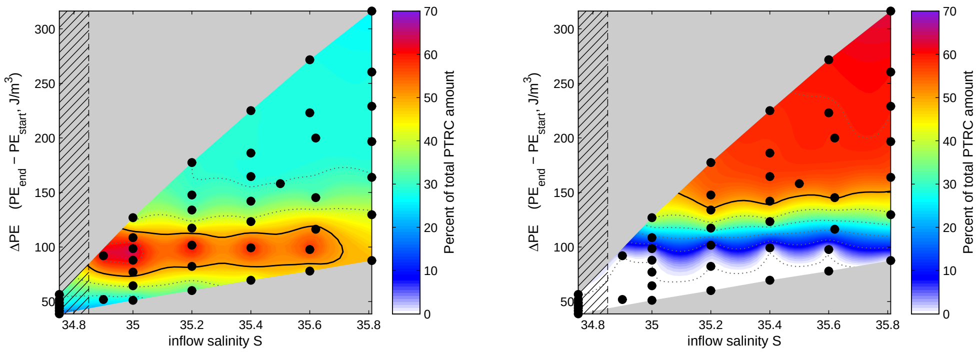

(a) $500\,\mathrm{m} \leq z \leq 1000\,\mathrm{m}$ (b) $z \geq 1000\,\mathrm{m}$

Figure 13: Similar to Fig. 11, but the percentage of tracer at a given depth range is plotted against S and ΔPE. Areas of untested S-ΔPE combinations are blanked.

In Fig. 13 we plot the final percentage of tracer mass found at the depth ranges 500-1000 m and 1000-1500 m against S and ΔPE. In contrast to Fig. 11 the contours of equal tracer percentage per depth range are now horizontal. This reveals that the cascading regime is a function of the potential energy gain ΔPE and independent of the inflow salinity and confirms that the initial density is not the only (or even the most significant) controlling parameter affecting the fate of the plume.

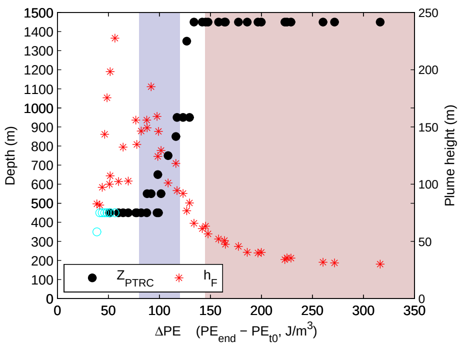

Figure 14: The depth level Z_{PTRC} at which the maximum amount of PTRC is found at the end of each run plotted against the gain in potential energy ΔPE (black bullets). Experiments with S=34.75 where the initial density is insufficient to penetrate the bottom layer are marked in cyan. Red stars show the average plume height h_F (in m) measured from tracer profiles. The approximate ΔPE ranges corresponding with arrested runs (light blue, cf. Fig. 13a) and piercing runs (light red, cf. Fig. 13b) are shaded.

The analysis is extended to more depth ranges and we compute M_{PTRC} in 100 m bins. The depth of the bin with the highest tracer mass gives Z_{PTRC} which is plotted against ΔPE in Fig. 14. The correlation between ΔPE and Z_{PTRC} (black bullets) shows very little scatter and indicates a functional relationship between the potential energy gain and the depth of penetration. With increasing potential energy in the system the plume is capable of first breaching the 200 m then the 500 m density interface in the ambient water. The abrupt transition from arrested ($Z_{\mathrm{PTRC}} \approx 500$ m) to piercing ($Z_{\mathrm{PTRC}} \approx 1500$ m) can be explained by the lack of stratification in the bottom layer. In most experiments where the plume breaches the AW-NSDW interface it also continues to the bottom of the slope after flowing through a homogenous layer of NSDW.

Using the buoyancy flux of a density current, a concept similar to the flux of potential energy, Wells and Nadarajah (2009) reported a functional dependence between the intrusion depth Z of a density current and the geostrophic buoyancy flux $B_{geo} = g'V_{Nof}h$ (where h is the initial height of the flow from a line source), the entrainment ratio E and the ambient buoyancy frequency N as $Z \sim E^{-\frac{1}{3}} B_{geo}^{\frac{1}{3}}/N$. However, their results are not readily applicable to our model which has non-linear ambient stratification with sharp density interfaces causing N to vary during the plume's descent. Neither is E constant during our experiments. In Fig. 14 we also plot the plume height h_F (red stars) against the potential energy gain ΔPE. It shows high h_F in runs with low ΔPE (those runs where the plume is arrested in the Atlantic Layer), and a low h_F in high-ΔPE runs when the plume spends little time transiting the AW and flows straight through to the NSDW layer.

The slow but steady rise in PE in Fig. 12 may suggest that any addition, however slow, of dense water (and thus potential energy) could eventually lead to the piercing regime if the initial SFOW density is greater than the density of the bottom layer (which is the case in our setup for $S>34.85$). Under this assumption the ΔPE-axis in Fig. 14 can be taken as a proxy for time. As time progresses (and ΔPE increases) the entrainment ratio E reduces (i.e. h_F shrinks) as the plume moves from the Atlantic Layer into the deep NSDW layer. When a certain threshold is passed, the plume has modified the ambient water sufficiently such that subsequent overflow waters pass through the AW relatively unimpeded (with less dilution) and penetrate into the deep waters. There is a caveat though, which works against the plume's piercing ability. The flow also needs to 'act quickly' (as is achieved by a high flow rate) to counteract mixing processes that cause the plume to dilute in the ambient waters.

4. Summary and conclusions

We perform a series of model experiments using idealised conical geometry and simplified ambient conditions to study the penetration of a dense water cascade into ambient stratification. The model setup was inspired by conditions previously observed at Svalbard in the Arctic Ocean. We investigate how variations in the parameters of the overflow - its initial salinity S and the flow rate Q - affect the fate of the plume.

We reproduce the main regimes where the plume is either (i) arrested at intermediate depths, (ii) pierces the intermediate layer and descends to the bottom of the continental slope or (iii) partially detaches off the bottom, intrudes into the intermediate layer while the remainder continues downslope.

Our results show that for our given model setup the regime is predictable from the initial source water properties - its density (typically given by the salinity S as the temperature is practically constant at near-freezing) and volume transport Q.

The results show that even a cascade with high initial salinity S may not pierce the Atlantic Layer if its flow rate Q is low. The initial density of the plume is therefore not the only parameter controlling the depth penetration of the plume. The combined effect of S and Q on the cascade's regime is explained by the system's gain in potential energy (ΔPE) arising from the introduction of dense water at shallow depth and a functional relationship exists between ΔPE and the penetration depth and thus the prevailing regime.

Acknowledgements

This work was partly funded by NERCs Core Research Programme Oceans 2025, the EU FP7 MyOcean/MyOcean2 project and a University of Plymouth PhD studentship. We thank Vladimir V. Ivanov (Scottish Association of Marine Science) for fruitful discussions regarding the vertical coordinate system. The National Centre for Ocean Forecasting (NCOF) provided us with the NEMO-SHELF code. Hedong Liu and Jason Holt (National Oceanography Centre, Liverpool) are acknowledged for kindly providing the code for the vertical PPM advection and the Pressure Jacobian horizontal pressure gradient schemes. H. Liu also assisted with the coding of the no-slip bottom boundary condition in NEMO. The authors would like to thank two anonymous reviewers for giving detailed comments and suggestions that have helped to improve the manuscript.

Appendix A. The s_h-coordinate system

The algorithm calculating the s-level depths at a given location with bathymetric depth D starts by adding levels in the bottom boundary layer equidistantly over a constant thickness H_{bbl}. The depths Z_h of the s_h-levels (the virtual seabeds) are then calculated based on the their prescribed depths Z_l according to the following scheme.

Let $D_{lim}(D) = D - H_{bbl} - k\,\Delta z_{min}$ be the deepest depth that the s_h-level can be placed at, where H_{bbl} is the thickness reserved for the bottom boundary layer, k is the number of levels between the s_h-level and the top of the bottom boundary layer, and Δz_{min} is the minimum allowable level spacing. This leads to a simple function

$$Z_h = \begin{cases} Z_l & , D_{lim} > Z_l \\ D_{lim} & , D_{lim} \leq Z_l \end{cases} \tag{A.1}$$

where the s_h-level is either horizontal ($Z_h = Z_l$) or terrain-following ($Z_h = D_{lim}$). As a consequence its first derivative is discontinuous in one point, which leads to errors in horizontal pressure gradient calculations where its second derivative is undefined.

In order to smoothly blend between these two cases, we start with a function S_0 that transitions smoothly between 1 to 0 whilst satisfying that $S_0(0.5) = 0.5$ (see blue curves in Fig. 3c):

$$S_0(x) = 0.5\, tanh(0.5\, \theta - x\, \theta) + 0.5 \tag{A.2}$$

where θ is a non-dimensional smoothing parameter. For values of approximately $2 \leq \theta \leq 20$ the transition is smooth, but as $\theta \to \infty$ the function becomes a step function (with a step at $x = 0.5$). Integrating Eq. (A.2) gives Eq. (A.3):

$$S_1(\alpha) = 0.5\, \alpha - \frac{0.5}{\theta}\, log\big(cosh(\theta - \alpha\, \theta)\big) + 0.5 - \frac{log(2)}{2\, \theta} \tag{A.3}$$

where $\alpha = Z_l / D_{lim}$ is a scale factor for the prescribed s_h-level depth Z_l. Eq. (A.3) approximately satisfies $S_1(\alpha) \approx \alpha$ for $0 \leq \alpha \leq 1$ and $S_1(\alpha) \approx 1$ for $\alpha > 1$ (see red curves in Fig. 3c) so it could be used to blend smoothly from $Z_h = Z_l$ at depth (using the range $\alpha \geq 1$) into $Z_h = D_{lim}$ in the shallows (using the range $0 \leq \alpha < 1$).

While Eq. (A.3) closely matches the identity function $f(x) = x$ in the approximate range $0 \leq x \leq 0.5$ it does not exactly do so, especially for small values of θ (see dashed red curve in Fig. 3c). The s_h-level could miss its target depth Z_l in the interior of the basin by a small margin, and a second smoothing function

$$S_2(\alpha) = \begin{cases} \alpha & , \alpha \leq 0.5 \\ 0.5 + 0.5\, tanh(2\, \alpha - 1) & , \alpha > 0.5 \end{cases} \tag{A.4}$$

is introduced to blend the identify function into Eq. (A.3). The final s_h-level depth Z_h is then derived as:

$$Z_h = D_{lim} \Big((1 - S_2)\, \alpha + S_2\, S_1 \Big) \tag{A.5}$$

For this study we use 16 levels in a bottom layer of constant thickness of 60 m resulting in a near-bottom vertical resolution of at least 3.75 m. The s_h-levels to coincide with the interfaces between the ambient water masses are placed at 200 and 500 m and a third s_h-level is inserted at 800 m to form a virtual sea bed for the levels below the deepest interface at 500 m. Vertical resolution in the interior ranges from 30 to 60 m (Figs. 3a and 3b).

The remaining s-levels are then evenly spaced within the gaps. The s_h-levels in this study are smoothed with values of θ equal to 4, 6 and 8 at the depths of 200, 500 and 800 m respectively.

Appendix B. Rotation of the lateral diffusion operator

Lateral diffusion processes occur predominantly along neutral surfaces (Griffies, 2004), which may not be easily characterised (in a well-mixed layer for example) and may be computationally expensive to derive, and are thus often approximated (see McDougall and Jackett, 2005, and references therein). Here we consider two such approximations for the slope m of operator rotation: (i) calculation of the slope of isopycnal surfaces $m_{iso} = \frac{d\rho}{dx} / \frac{d\rho}{dz}$, and (ii) calculation of the slope m_{hor} of near-horizontal surfaces of constant geopotential derived from the time-evolving elevation of the sea surface.

The rotation of the diffusion operator according to m_{iso} is generally preferred in shelf seas models (H. Liu, pers. comm., 2012) where density gradients are generally well defined by prevalent stratification. However, in mixed layers of insignificant density gradients the calculation of m_{iso} can lead to unphysical fluctuations in the slope. The rotation of the diffusion operator is therefore limited to a maximum slope angle $m_{max} = 0.028$ which reflects the 1.8 ° inclination of our model topography[2]. Even with this safeguard in

[2]The slope limit m_{max} can be approximated from the typical length scale L and depth scale H of the diffusion process: $m_{max} = \frac{H}{L}$. NEMO typically uses a value of $m_{max} = 0.01$ which is not suitable for steep topographical gradients in our scenario. This original value was derived for large-scale ocean models with a typical mixed layer depth of $H = 200$ m. The length scale of lateral diffusion $L_{A_h} = 20$ km is in turn derived from a typical horizontal diffusion coefficient $A_h = 2000\,\mathrm{m^2 s^{-1}}$ while assuming a typical horizontal velocity of $10\,\mathrm{cm\,s^{-1}}$).

place the analytical description of our ambient density profile can lead to numerically spurious slopes within a well-mixed layer and the use of the m_{hor} slopes would be preferable in that case.

For this study we therefore adopt a blended scheme where the Laplacian diffusion operator is rotated according to m_{iso} in stratified regions and according to m_{hor} in well-mixed regions. We assess here the degree of stratification via the buoyancy frequency N^2 which is a NEMO model variable. Two additional parameters ${N^2}_{hor}$ and ${N^2}_{iso}$ are introduced in our configuration to define the lower limit of the buoyancy frequency below which we use m_{hor} and above which we use m_{iso}, while intermediate values are linearly interpolated. The final slope m for the rotation of the Laplacian diffusion operator is calculated as:

$$\begin{aligned} \alpha &= min\left(1, \frac{max\big(0, (N^2 - {N^2}_{hor})\big)}{{N^2}_{iso} - {N^2}_{hor}}\right) \\ m &= (1-\alpha)\cdot m_{hor} + \alpha\cdot m_{iso} \end{aligned} \tag{B.1}$$

While it may be possible to calculate suitable limits without prior knowledge, we derived ${N^2}_{hor} = 5\times10^{-6}\,\mathrm{s}^{-2}$ and ${N^2}_{iso} = 5\times10^{-5}\,\mathrm{s}^{-2}$ by visually inspecting cross-section plots of N^2. In keeping with the standard NEMO code, we apply a 2D Shapiro-filter to the final values of m and additionally reduce them by 50% near coastal boundaries. Furthermore, the code that specially adapts lateral diffusion in model levels within and just below the surface mixed layer was removed.

References

Aagaard, K., Coachman, L.K., Carmack, E.C., 1981. On the halocline of the arctic ocean. Deep Sea Research Part A. Oceanographic Research Papers 28, 529–545.

Aagaard, K., Swift, J.H., Carmack, E.C., 1985. Thermohaline circulation in the arctic mediterranean seas. Journal of Geophysical Research 90, 4833–4846.

Akimova, A., Schauer, U., Danilov, S., Núñez-Riboni, I., 2011. The role of the deep mixing in the storfjorden shelf water plume. Deep Sea Research Part I: Oceanographic Research Papers 58, 403–414.

Cavalieri, D.J., Martin, S., 1994. The contribution of alaskan, siberian and canadian coastal polynyas to the halocline layer of the arctic ocean. Journal of Geophysical Research 99, 18343–18362.

Conkright, M.E., Locarnini, R.A., Garcia, H.E., OBrien, T.D., Boyer, T.P., Stephens, C., Antonov, J.I., 2002. World Ocean Atlas 2001: Objective Analyses, Data Statistics, and Figures, CDROM Documentation. Technical Report. National Oceanographic Data Center, Silver Spring, MD.

Cushman-Roisin, B., Beckers, J.M., 2011. Introduction to Geophysical Fluid Dynamics, 2nd Edition - Physical and Numerical Aspects. Academic Press.

Enriquez, C.E., Shapiro, G.I., Souza, A.J., Zatsepin, A.G., 2005. Hydrodynamic modelling of mesoscale eddies in the black sea. Ocean Dynamics 55, 476–489.

Fer, I., Ådlandsvik, B., 2008. Descent and mixing of the overflow plume from storfjord in svalbard: an idealized numerical model study. Ocean Science 4, 115–132.

Fer, I., Skogseth, R., Haugan, P.M., Jaccard, P., 2003. Observations of the storfjorden overflow. Deep Sea Research Part I: Oceanographic Research Papers 50, 1283–1303.

Geyer, F., Fer, I., Eldevik, T., 2009. Dense overflow from an arctic fjord: Mean seasonal cycle, variability and wind influence. Continental Shelf Research 29, 2110–2121.

Griffies, S.M., 2004. Fundamentals of Ocean Climate Models. Princeton University Press.

Griffiths, R.W., Linden, P.F., 1982. Laboratory experiments on fronts. part 1 density-driven boundary currents. Geophysical and Astrophysical Fluid Dynamics 19, 159–187.

Haarpaintner, J., Gascard, J.C., Haugan, P.M., 2001. Ice production and brine formation in storfjorden, svalbard. Journal of Geophysical Research: Oceans 106, 14001–14013.

Haney, R.L., 1991. On the pressure gradient force over steep topography in sigma coordinate ocean models. Journal of Physical Oceanography 21, 610–619.

Holt, J., Umlauf, L., 2008. Modelling the tidal mixing fronts and seasonal stratification of the northwest european continental shelf. Continental Shelf Research 28, 887–903.

Ilıcak, M., Adcroft, A.J., Griffies, S.M., Hallberg, R.W., 2012. Spurious dianeutral mixing and the role of momentum closure. Ocean Modelling 45–46, 37–58.

Ivanov, V., 2011. How summer ice depletion in the arctic ocean may affect the global thc? Geophysical Research Abstracts 13, EGU2011–4457.

Ivanov, V.V., Shapiro, G.I., Huthnance, J.M., Aleynik, D.L., Golovin, P.N., 2004. Cascades of dense water around the world ocean. Progress In Oceanography 60, 47–98.

Jakobsson, M., Macnab, R., Mayer, L., Anderson, R., Edwards, M., Hatzky, J., Schenke, H.W., Johnson, P., 2008. An improved bathymetric portrayal of the arctic ocean: Implications for ocean modeling and geological, geophysical and oceanographic analyses. Geophysical Research Letters 35, L07602.

Jungclaus, J.H., Backhaus, J.O., Fohrmann, H., 1995. Outflow of dense water from the storfjord in svalbard: A numerical model study. Journal of Geophysical Research 100, 24719–24728.

Kämpf, J., 2005. Cascading-driven upwelling in submarine canyons at high latitudes. Journal of Geophysical Research 110, C02007.

Killworth, P.D., 2001. On the rate of descent of overflows. Journal of Geophysical Research 106, 22267–22275.

Levier, B., Treguier, A.M., Madec, G., Garnier, V., 2007. Free surface and variable volume in the nemo code, MERSEA IP report WP09-CNRSSTR-03-1A. Technical Report. Laboratoire de Physique des Oceans, Brest.

Liu, H., Holt, J., 2010. Combination of the Vertical PPM Advection Scheme with the Existing Horizontal Advection Schemes in NEMO. MyOcean Science Days, 1-3 December 2010, Météo-France International Conference Center Toulouse, France. http://mercator-myoceanv2.netaktiv.com/MSD_2010/Abstract/Abstract_LIUhedong_MSD_2010.doc.

Madec, G., 2008. NEMO ocean engine. Note du Pôle de modélisation. Technical Report No. 27. Institut Pierre-Simon Laplace (IPSL), France. ISSN: 1288-1619.

McDougall, T.J., Jackett, D.R., 2005. The material derivative of neutral density. Journal of Marine Research 63, 159–185.

Mellor, G.L., Ezer, T., Oey, L.Y., 1994. The pressure gradient conundrum of sigma coordinate ocean models. Journal of Atmospheric and Oceanic Technology 11, 1126–1134.

Nof, D., 1983. The translation of isolated cold eddies on a sloping bottom. Deep Sea Research Part A. Oceanographic Research Papers 30, 171–182.

O'Dea, E.J., Arnold, A.K., Edwards, K.P., Furner, R., Hyder, P., Martin, M.J., Siddorn, J.R., Storkey, D., While, J., Holt, J.T., Liu, H., 2012. An operational ocean forecast system incorporating nemo and sst data assimilation for the tidally driven european north-west shelf. Journal of Operational Oceanography 5, 3–17.

Quadfasel, D., Rudels, B., Kurz, K., 1988. Outflow of dense water from a svalbard fjord into the fram strait. Deep Sea Research Part A. Oceanographic Research Papers 35, 1143–1150.

Rudels, B., Björk, G., Nilsson, J., Lake, I., Nohr, C., 2005. The interactions between waters from the arctic ocean and the nordic seas north of fram strait and along the east greenland current: results from the arctic ocean-02 oden expedition. Journal of Marine Systems 55, 1–30.

Rudels, B., Jones, E.P., Anderson, L.G., Kattner, G., 1994. On the intermediate depth waters of the arctic ocean, in: Johannessen, O.M., Muench, R.D., Overland, J.E. (Eds.), The Polar Oceans and their role in shaping the global environment. American Geophysical Union, Washington, D.C.. volume Geophysical Monograph 85, pp. 33–46.

Rudels, B., Quadfasel, D., 1991. Convection and deep water formation in the arctic ocean-greenland sea system. Journal of Marine Systems 2, 435–450.

Saloranta, T.M., Haugan, P.M., 2004. Northward cooling and freshening of the warm core of the west spitsbergen current. Polar Research 23, 79–88.

Schauer, U., 1995. The release of brine-enriched shelf water from storfjord into the norwegian sea. Journal of Geophysical Research 100, 16015–16028.

Schauer, U., Fahrbach, E., 1999. A dense bottom water plume in the western barents sea: downstream modification and interannual variability. Deep Sea Research Part I: Oceanographic Research Papers 46, 2095–2108.

Schauer, U., Rudels, B., Fer, I., Haugan, P.M., Skogseth, R., Björk, G., Winsor, P., 2003. Return of deep shelf/slope convection in the western barents sea?, in: Seventh Conference on Polar Meteorology and Oceanography and Joint Symposium on High-Latitude Climate Variations, The American Meteorological Society, Hyannis, MA.

Shapiro, G.I., Hill, A.E., 1997. Dynamics of dense water cascades at the shelf edge. Journal of Physical Oceanography 27, 2381–2394.

Shapiro, G.I., Huthnance, J.M., Ivanov, V.V., 2003. Dense water cascading off the continental shelf. Journal of Geophysical Research 108, 3390–3409.

Shapiro, G.I., Zatsepin, A.G., 1997. Gravity current down a steeply inclined slope in a rotating fluid. Annales Geophysicae 15, 366–374.

Skogseth, R., Fer, I., Haugan, P.M., 2005a. Dense-water production and overflow from an arctic coastal polynya in storfjorden, in: Drange, H., Dokken, T., Furevik, T., Gerdes, R., Berger, W. (Eds.), The Nordic Seas: An Integrated Perspective. AGU Geophysical Monograph Series 158. American Geophysical Union, pp. 73–88.

Skogseth, R., Haugan, P.M., Jakobsson, M., 2005b. Watermass transformations in storfjorden. Continental Shelf Research 25, 667–695.

Smethie, W.M., Ostlund, H.G., Loosli, H.H., 1986. Ventilation of the deep greenland and norwegian seas: Evidence from krypton-85, tritium, carbon-14, and argon-39. Deep Sea Research Part A. Oceanographic Research Papers 33, 675–703.

Song, Y., Haidvogel, D., 1994. A semi-implicit ocean circulation model using a generalized topography-following coordinate system. Journal of Computational Physics 115, 228–244.

Turner, J.S., 1986. Turbulent entrainment: the development of the entrainment assumption, and its application to geophysical flows. Journal of Fluid Mechanics 173, 431–471.

Umlauf, L., Burchard, H., 2003. A generic length-scale equation for geophysical turbulence models. Journal of Marine Research 61, 235–265.

Warner, J.C., Sherwood, C.R., Arango, H.G., Signell, R.P., 2005. Performance of four turbulence closure models implemented using a generic length scale method. Ocean Modelling 8, 81–113.

Wells, M.G., Nadarajah, P., 2009. The intrusion depth of density currents flowing into stratified water bodies. Journal of Physical Oceanography 39, 1935–1947.

Winters, K.B., Lombard, P.N., Riley, J.J., D'Asaro, E.A., 1995. Available potential energy and mixing in density-stratified fluids. Journal of Fluid Mechanics 289, 115–128.

Wobus, F., Shapiro, G.I., Maqueda, M.A.M., Huthnance, J.M., 2011. Numerical simulations of dense water cascading on a steep slope. Journal of Marine Research 69, 391–415.